

Spectrally accurate reverse-mode differentiable bounce-averaging operator and its applications

K. Unalmis^{1†}, R. Gaur², R. Conlin³, D. Panici², and E. Kolemen^{2,4}

¹Electrical and Computer Engineering, Princeton University, NJ 08544, USA

²Mechanical and Aerospace Engineering, Princeton University, NJ 08544, USA

³IREAP, University of Maryland, College Park, MD 20740, USA

⁴Princeton Plasma Physics Laboratory, Princeton, NJ, USA

(Received xx; revised xx; accepted xx)

We present a spectrally accurate bounce-averaging operator implemented as a part of the automatically differentiable DESC stellarator optimization suite. Using this operator, we calculate the proxy for neoclassical transport coefficient $\epsilon_{\text{eff}}^{3/2}$ in the $1/\nu$ regime and benchmark it against the NEO code. Ultimately, by employing this differentiable approximation, for the first time, we directly optimize a finite- β stellarator to enhance neoclassical transport using reverse-mode differentiation. This ensures that the computational cost of determining the gradients does not depend on the number of input parameters.

1. Introduction

Stellarators, first conceived by Spitzer Jr (1958), represent a distinct approach to magnetic confinement fusion that offers unique advantages over tokamaks. These toroidal devices achieve plasma confinement through external magnetic fields rather than through plasma current, providing greater design flexibility and operational stability. The absence of toroidal symmetry allows for magnetic field optimization through boundary shaping, which helps minimize the net toroidal current and thereby avoid the current-driven plasma instabilities and disruptions that plague tokamak operation (Helander 2014).

The design of optimal stellarator configurations is a complex optimization problem involving hundreds of degrees of freedom. Traditional optimization approaches have evolved significantly over the past decades. The VMEC (Variational Moments Equilibrium Code), developed by Hirshman & Whitson (1983), has served as the foundation for numerous stellarator optimization efforts. Building upon VMEC, several optimization frameworks have emerged: STELLOPT Lazerson *et al.* (2020), which implements a suite of physics-based optimization criteria; ROSE (Drevlak *et al.* 2018), which focuses on coil optimization and engineering constraints; and more recently, SIMSOPT (Landreman *et al.* 2021), which provides a flexible approach to stellarator optimization.

However, in general, traditional approaches rely on finite-difference techniques to compute gradients. Such techniques may not yield an accurate estimate of the gradient which can affect the optimizer convergence. Furthermore, the objective function must be recomputed to estimate the gradient for each optimizable parameter. In DESC, unlike previous optimizers, it is not necessary to resolve the MHD force balance equation at each optimization step. Additional objectives that depend on equilibrium force balance can be optimized simultaneously on a single device while ensuring ideal MHD force balance.

In this paper we present a fast, automatically-differentiable bounce-averaging operator which is used to simplify kinetic models such as drift and gyrokinetics. Specifically, we

† Email address for correspondence: kunalmis@princeton.edu, ekolemen@princeton.edu

will focus on neoclassical transport in the $1/\nu$ regime by evaluating and optimizing for the effective ripple [Nemov *et al.* \(1999\)](#). The bounce-averaging operators and drift kinetic model is explained in the following sections. This operator is implemented as a part of the DESC [Dudt & Kolemen \(2020\)](#); [Panici *et al.* \(2023\)](#); [Conlin *et al.* \(2023\)](#) optimization suite.

In section 2, we will briefly explain how we solve the ideal MHD equation and calculate an equilibrium using the DESC suite. In section 3, we will introduce the drift kinetic model and explain the derivation of neoclassical transport in the $1/\nu$ collisionality regime, as done by Nemov and present comparison of the effective ripple with the NEO code from the STELLOPT suite for various stellarator equilibria. In section 4, we explain our implementation of the reverse-mode differentiable proxy and demonstrate how it is faster than forward-mode calculation. In section 5, we optimize equilibria against neoclassical transport. In section 6, we conclude our work and explain how it can be extended.

2. Ideal MHD equilibrium

Our study only concerns solutions whose magnetic field lines lie on closed nested toroidal surfaces, known as flux surfaces. We label the flux surfaces with their enclosed toroidal flux ψ . On each flux surface, curves of constant α correspond to magnetic field lines. A divergence-free magnetic field can be written in the Clebsch form ([D’haeseleer *et al.* 2012](#))

$$\mathbf{B} = \nabla\psi \times \nabla\alpha. \quad (2.1)$$

In a set of specialized coordinates, known as flux coordinates, $\alpha = \vartheta - \iota\phi$ where ϑ is a PEST poloidal angle, ϕ is the cylindrical coordinate from the coordinate system (R, ϕ, Z) , and the quantity

$$\iota = \frac{\mathbf{B} \cdot \nabla\vartheta}{\mathbf{B} \cdot \nabla\phi}, \quad (2.2)$$

is the pitch of the field line on a flux surface, commonly referred to as the rotational transform. The definition of \mathbf{B} in (2.1) is consistent with (2.2).

We solve the steady-state, ideal MHD (MagnetoHydroDynamic) equation

$$\nabla \left(\mu_0 p + \frac{B^2}{2} \right) = \mathbf{B} \cdot \nabla \mathbf{B} \quad (2.3)$$

which describes a balance between the plasma pressure p , magnetic field pressure B^2 and the effect of field line curvature $\mathbf{B} \cdot \nabla \mathbf{B}$. Unlike a tokamak, we cannot simplify (2.3) to a two-dimensional scalar Grad-Shafranov equation. Assuming the existence of nested flux surfaces, we can only reduce (2.3) to two coupled three-dimensional equations. All terms in (2.3) are represented using a Fourier-Zernike spectral representation. This representation allows for efficient computation of derivatives, ensures smoothness of the solution and regularity near the magnetic axis [Dudt & Kolemen \(2020\)](#); [Panici *et al.* \(2023\)](#). This boundary value problem is then solved as a minimization problem using a trust-region method. Since DESC is written in JAX, we typically accelerate our computation on a GPU. All calculations presented in this paper are performed on an NVIDIA A100 GPU.

3. Neoclassical model of plasma

The dynamics of a magnetized hot plasma differs significantly from that of an unmagnetized fluid. Unlike isotropic hard-sphere collisions that govern the behavior of an uncharged fluid, a plasma behaves differently in directions perpendicular and parallel to

the magnetic field lines because of Coulomb collisions. In magnetized plasmas, particles traverse helical trajectories around magnetic field lines, exhibiting motion characterized by gyration around these lines and drifts across them. The classical transport model assumes a simplistic view of particle collisions and does not adequately incorporate the effects of these drifts. To correctly account for the effect of drifts, trapped and passing particles, and the magnetic geometry, we use the neoclassical transport theory.

There are three fundamental length and time scales relevant to magnetized plasmas. The time scales correspond to the particle transit frequency $v_{\text{th},s}/L$, where $v_{\text{th},s} = \sqrt{2T_s/m_s}$ is the thermal speed, the Coulomb collision frequency $\nu_{ss'} \propto T^{3/2}$, and the gyration (cyclotron) frequency $\Omega_s = Z_s e B / (m_s c)$ where s, s' are the species of interest. For each time scale, the corresponding length scales are the gradient scale length of the magnetic field L , the mean free path λ_{mfp} , and the gyroradius $\rho_s = v_{\text{th},s}/\Omega_s$, respectively. In a magnetized plasma,

$$\nu_{ss'} \sim \frac{v_{\text{th},s}}{L} \ll \Omega_s, \quad \lambda_{\text{mfp}} \sim L \gg \rho_s. \quad (3.1)$$

Using a random walk estimate, we can calculate the classical heat transport coefficient in the perpendicular direction as $D_{\perp} \sim \nu_{ss'} \rho_s^2 \sim T^{5/2}$ (Helander & Sigmar 2005) whereas, using neoclassical theory, we have $\Delta x \sim \rho(B/B_p)$, B and B_p are the total and poloidal magnetic field strength, respectively which gives $D_{\perp} \sim \nu_{ss'} \rho_s^2 (B/B_p)^2 \sim T^{5/2} (B/B_p)^2$. The ratio B/B_p strongly depends on the magnetic field geometry and can significantly affect the regime of neoclassical transport.

A magnetized plasma can either be weakly or strongly collisional. This is defined by the collisionality $\nu_* \equiv \lambda_{\text{mfp}}/L = \nu/(v_{\text{th},s}/L)$. In a strongly collisional plasma, particles undergo frequent collisions without covering a significant distance along a magnetic field line, *i.e.*, $\nu_* \gg 1$. Conversely, in a weakly collisional plasma, particles can traverse and move along the field line multiple times before colliding, *i.e.*, $\nu_* \ll 1$. Stellarator plasmas in practical applications tend to be weakly collisional.

Based on the stellarator geometry, the weak collisionality regime can be further divided into the banana or plateau regime depending on the inverse aspect ratio $\epsilon \sim q/(B/B_p)$. Most stellarators lie in the banana regime, where the collisionality $\nu_* \ll \epsilon^{3/2}$. Therefore, we want to minimize neoclassical transport in the banana regime. This categorization is illustrated in figure 1.

For the banana regime, Nemov *et al.* (1999) first derived a simplified form of the effective ripple proxy by systematically simplifying the Neoclassical equation. This process is explained in the following section.

3.1. Effective ripple

In this section, we explain in detail, the derivation of the effective field ripple similar to the one used by Nemov *et al.* (1999) In the limit of low collisionality $\nu_* \ll \epsilon^{3/2}$, neoclassical model studies the distribution of plasma determined by the solving the drift-kinetic equation

$$v_{\parallel} \mathbf{b} \cdot \nabla F_1 + \mathbf{v}_{\text{Ds}} \cdot \nabla F_0 = \mathcal{C}[F_1] \quad (3.2)$$

where $F_0 = F_0(\psi, \alpha, E)$ is a background Maxwellian distribution function, $F_1 = F_1(\psi, \alpha, E, \mu)$ is the higher-order correction over the Maxwellian, and \mathcal{C} the Lorenz or pitch-angle scattering collision operator

$$\mathcal{C}[F_1] = m\nu(E)v_{\parallel} \left. \frac{\partial}{\partial \mu} \right|_E \left. \frac{\mu v_{\parallel}}{|B|} \frac{\partial F_1}{\partial \mu} \right|_E \quad (3.3)$$

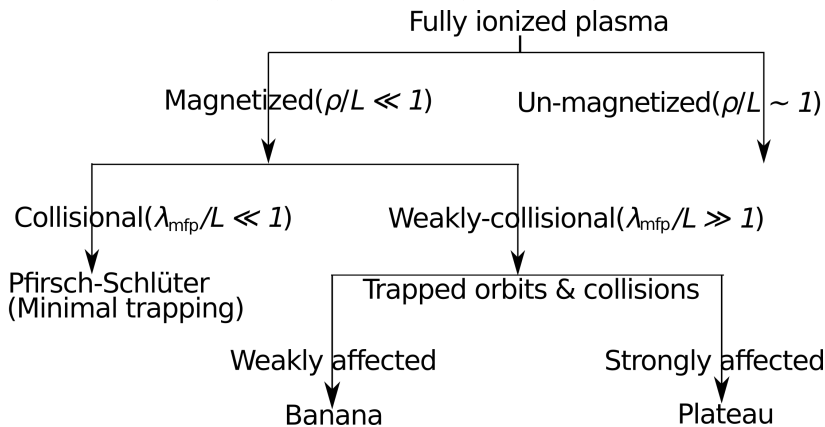


Figure 1: Schematic categorizing neoclassical transport in a fully ionized plasma. Most stellarators fusion power plant designs lie in the banana regime. Hence, we use the effective ripple, a proxy that quantifies neoclassical transport in the banana regime.

where ν is the collision frequency, $E = mv^2/2$ is total kinetic energy of a particle. Often, the Lorenz operator is also written in terms of the pitch angle $\lambda = \mu/E$. Also, define

$$\mathbf{v}_{Ds} = \frac{1}{\Omega_s} \left[v_{\parallel}^2 \mathbf{b} \times (\mathbf{b} \cdot \nabla \mathbf{b}) + \frac{v_{\perp}^2}{2B} \mathbf{b} \times \nabla |B| \right] \quad (3.4)$$

$$\Omega_s = \frac{Z_s e |B|}{m_s c} \quad (3.5)$$

Note that we have ignored the effect of the electric field in the drift-kinetic equation. To further simplify the equation, we average the bounce motion of the particles by applying the bounce averaging operator for a particle with a fixed pitch angle

$$\bar{X} = \oint \frac{d\ell}{v_{\parallel}} X \Big/ \oint \frac{d\ell}{v_{\parallel}} \quad (3.6)$$

where l is the length along the field line and v_{\parallel} is the parallel speed of a particle and the bounce-averaging operator is applied at a constant λ . Using the streamline property of a magnetic field

$$\frac{d\ell}{|B|} = \frac{d\zeta}{\mathbf{B} \cdot \nabla \zeta} = \frac{d\theta}{\mathbf{B} \cdot \nabla \theta}, \quad (3.7)$$

in the curvilinear coordinate system (ρ, θ, ζ) , we can re-write the bounce averaging operator

$$\bar{X} = \oint \frac{d\zeta}{(\mathbf{b} \cdot \nabla \zeta)} \frac{1}{v_{\parallel}} X \Big/ \oint \frac{d\zeta}{(\mathbf{b} \cdot \nabla \zeta)} \frac{1}{v_{\parallel}} \quad (3.8)$$

Applying the bounce-averaging operator to (3.2), we get

$$\overline{\mathbf{v}_{Ds} \cdot \nabla \alpha} \frac{\partial F_0}{\partial \alpha} + \overline{\mathbf{v}_{Ds} \cdot \nabla \psi} \frac{\partial F_0}{\partial \psi} = m\nu(E) \frac{\partial}{\partial \mu} \mu I \frac{\partial F_1}{\partial \mu} \quad (3.9)$$

where $I = \overline{v_{\parallel}/B}$. Assuming that the binormal component of the magnetic drift $\overline{\mathbf{v}_{D_s} \cdot \nabla \alpha} \ll \overline{\mathbf{v}_{D_s} \cdot \nabla \psi}$ gives us a simplified bounce-averaged neoclassical equation

$$\overline{\mathbf{v}_{D_s} \cdot \nabla \psi} \frac{\partial F_0}{\partial \psi} = m\nu(E) \frac{\partial}{\partial \mu} \mu I \frac{\partial F_1}{\partial \mu} \quad (3.10)$$

To invert the collision operator, we can use the following identity

$$\mathbf{v}_{D_s} \cdot \nabla \psi = -\frac{v_{\parallel}}{3} \frac{\partial}{\partial \mu} \Big|_{E, \mathbf{r}} (3v^2 v_{\parallel} + v_{\parallel}^3) \frac{\kappa_G}{\Omega_s} \quad (3.11)$$

$$v_{\parallel} = \sqrt{\frac{2(E - \mu|B|)}{m}} \quad (3.12)$$

where the geodesic curvature $\kappa_G = [\mathbf{b} \times (\mathbf{b} \cdot \nabla \mathbf{b})] \cdot \nabla \psi$ and we have used the ideal MHD force balance equation (2.3). Using the identity, we can rewrite (3.10)

$$-\frac{1}{3} \frac{\partial}{\partial \mu} \left\{ \oint \left[\frac{d\zeta}{\mathbf{b} \cdot \nabla \zeta} (3v^2 v_{\parallel} + v_{\parallel}^3) \frac{\kappa_G}{\Omega_s} \frac{\partial F_0}{\partial \psi} \right] / \oint \frac{d\zeta}{(\mathbf{b} \cdot \nabla \zeta)} \frac{1}{v_{\parallel}} \right\} = \frac{\partial}{\partial \mu} \left[m\nu\mu I \frac{\partial F_1}{\partial \mu} \right] \quad (3.13)$$

We can now integrate above equation in μ and obtain

$$\frac{\partial F_1}{\partial \mu} = -\frac{H}{3m\nu\mu I} \frac{\partial F_0}{\partial \psi} \quad (3.14)$$

$$H = \oint \left[\frac{d\zeta}{\mathbf{b} \cdot \nabla \zeta} (3v^2 v_{\parallel} + v_{\parallel}^3) \frac{\kappa_G}{\Omega_s} \right] / \oint \frac{d\zeta}{(\mathbf{b} \cdot \nabla \zeta)} \frac{1}{v_{\parallel}} \quad (3.15)$$

We want to minimize the flux surface averaged radial particle flux

$$\Gamma = \oint \frac{dS}{|\nabla \psi|} \int d^3 \mathbf{v} (\mathbf{v}_{D_s} \cdot \nabla \psi) F_1 \quad (3.16)$$

$$= -\oint \frac{dS}{|\nabla \psi|} \int d^3 \mathbf{v} \frac{v_{\parallel}}{3} \frac{\partial}{\partial \mu} (3v^2 v_{\parallel} + v_{\parallel}^3) \frac{\kappa_G}{\Omega_s} F_1 \quad (3.17)$$

We shall use two different coordinate representations of the velocity integral: (E, μ, ϑ) , and $(E, \hat{\lambda}B_0, \vartheta) = (E, b', \vartheta)$.

$$\begin{aligned} \int d^3 \mathbf{v} &= 2\pi|B| \int_0^\infty dE \int_0^E \frac{d\mu}{|v_{\parallel}|} \\ &= 2\pi \sum_{\sigma} \int dE \sqrt{E} \int \frac{d\hat{\lambda}|B|}{\sqrt{1 - \hat{\lambda}|B|}} \\ &= -2\pi \sum_{\sigma} \int dE \sqrt{E} \int \frac{|B|}{B_0} \frac{db'}{b'^2 \sqrt{1 - |B|/(B_0 b)}} \end{aligned} \quad (3.18)$$

Rewriting the velocity integral in (E, μ, ϑ) and using integration of parts in the μ coordinate and using the boundary condition $\lim_{v_{\parallel} \rightarrow \infty} F_1 = 0$ we can rewrite the particle flux

$$\Gamma = \left(\int \frac{d\zeta}{\mathbf{b} \cdot \nabla \zeta} |\nabla \psi| \right)^{-1} \int d^3 \mathbf{v} H \frac{\partial F_1}{\partial \mu}. \quad (3.19)$$

Finally, we redefine $\partial F_0 / \partial \psi = \partial F_0 / \partial r (\int d\zeta / (\mathbf{b} \cdot \nabla \zeta) / \int d\zeta / (\mathbf{b} \cdot \nabla \zeta) |\nabla \psi|)$ in (3.15) and rewrite the velocity integral in (E, b', ϑ) and get the following form

$$\Gamma = \epsilon_{\text{eff}}^{3/2} \int dE E^{3/2} \int db' \frac{\hat{H}^2}{\hat{I}} \quad (3.20)$$

$$\epsilon_{\text{eff}}^{3/2} = \frac{\pi R^2}{8\sqrt{2}} \lim_{l \rightarrow \infty} \left(\int_0^{L_s} \frac{dl}{|B|} \right) \left(\int_0^L \frac{dl}{|B|} |\nabla\psi| \right)^{-2} \int_{B_{\text{max}}}^{B_{\text{min}}} db' \sum_{j=1}^{j_{\text{max}}} \frac{\hat{H}_j^2}{\hat{I}_j} \quad (3.21)$$

Since $\epsilon_h^{3/2}$ is a purely geometry dependent term, reducing it by varying the stellarator plasma boundary can reduce the radial neoclassical loss of the trapped particles.

To ensure low neoclassical transport and high performance, we typically optimize a stellarator so that it has a ripple $\epsilon_{\text{eff}} < 2\%$ which corresponds to a $\epsilon_{\text{eff}}^{3/2} < 0.003$. Throughout this paper, we will plot $\epsilon_{\text{eff}}^{3/2}$. In section 4.1, we compare the transport coefficient values calculated using DESC against the transport coefficient NEO code, for various stellarator configurations.

4. Reverse-mode differentiable bounce-averaging

To obtain the effective ripple, we calculate a set of bounce integrals throughout the plasma volume and integrate over the inverse pitch angle. In summary, there are three parts to this calculation.

- (i) Calculating the physical quantities using equilibrium parameters. For the magnetic field, we use the notation $B = B(\mathbf{p}_i)$.
- (ii) Root finding pairs of bounce points $\zeta_j = g(b'_0, B)$ for a given inverse pitch angle b'_0 .
- (iii) Calculating the bounce integrals, surface integral, and integrals in the inverse pitch angle b' to obtain $\epsilon_{\text{eff}}^{3/2} = (\epsilon_{\text{eff}}(\zeta_j))^{3/2}$.

Since the bounce averaging is defined to lie on a flux surface, the physical quantities are approximated with a double Fourier series in (θ, ζ) on each flux surface. The mapping from the curvilinear flux coordinates (ρ, θ, ζ) to the Clebsch field line coordinates (ρ, α, ζ) is approximated with Fourier-Chebyshev series on each flux surface. Appendix A explains the function approximation techniques in more detail. The velocity space grid is discretized with $N_{b'}$ uniformly spaced values of an inverse pitch angle coordinate $b' \in [\min(B)/B_0, \max(B)/B_0]$. A global root-finding algorithm with resolution labeled by Y_B computes the bounce points over N_l toroidal transits of the field line. These bounce points are the values of (ρ, α, ζ) where $v_{\parallel} = 0$, or equivalently, where $\lambda|B|(\rho, \alpha, \zeta) = 1$ for some field line specified by some (ρ, α) . High-order quadratures with resolution N_q estimate the bounce averages. Justification of the quadrature to compute the bounce averages are given in Appendix B.

In a forward mode operation, the derivative

$$\frac{\partial \epsilon_{\text{eff}}^{3/2}}{\partial \mathbf{p}_i} = \frac{\partial B}{\partial \mathbf{p}_i} \frac{\partial \zeta_j}{\partial B} \frac{\partial \epsilon_{\text{eff}}}{\partial \zeta_i} \frac{\partial \epsilon_{\text{eff}}^{3/2}}{\partial \epsilon_{\text{eff}}} \quad (4.1)$$

is calculated using a chain rule. For each variable, `jax` defines the sequence of operations and calculates the partial derivatives. This chain rule must be performed separately for each parameter and scales with the number of parameters $N_{\mathbf{p}}$. In a realistic stellarator optimization, $N_{\mathbf{p}} \sim (10^2 - 10^3)$. On the other hand, for a reverse-mode operation, we first do a single forward pass to store the order and structure of operators and all the intermediate functions without calculating any derivatives and then sequentially do the following operations

$$\frac{\partial \epsilon_{\text{eff}}^{3/2}}{\partial \epsilon_{\text{eff}}} = \frac{3}{2} \rightarrow \frac{\partial \epsilon_{\text{eff}}^{3/2}}{\partial \zeta_i} = \frac{\partial \epsilon_{\text{eff}}^{3/2}}{\partial \epsilon_{\text{eff}}} \frac{\partial \epsilon_{\text{eff}}}{\partial \zeta_j} \rightarrow \frac{\partial \epsilon_{\text{eff}}^{3/2}}{\partial B} = \frac{\partial \epsilon_{\text{eff}}^{3/2}}{\partial \zeta_i} \frac{\partial \zeta_j}{\partial B} \rightarrow \frac{\partial \epsilon_{\text{eff}}^{3/2}}{\partial \mathbf{p}_i} = \frac{\partial \epsilon_{\text{eff}}^{3/2}}{\partial B} \frac{\partial B}{\partial \mathbf{p}_i} \quad (4.2)$$

Thus, by utilizing the inverse approach, the chain rule relies solely on the output variable's

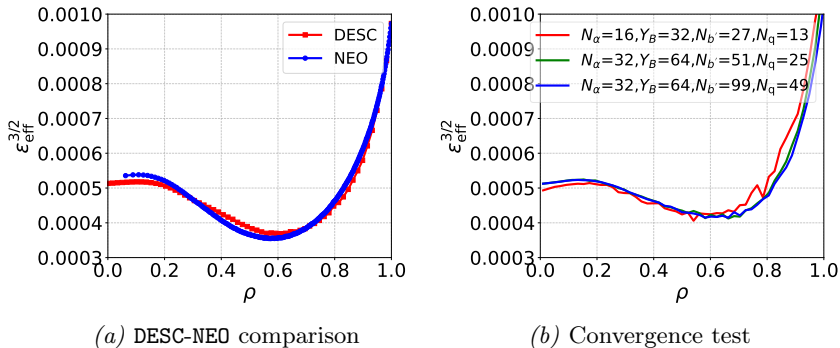


Figure 2: Figure (a) shows a comparison of the neoclassical transport coefficient $\epsilon_{\text{eff}}^{3/2}$ between DESC and NEO for the standard W7-X configuration whereas figure (b) shows a resolution scan of the $\epsilon_{\text{eff}}^{3/2}$. DESC and NEO agree reasonably well.

dimension, which, in the case of ϵ_{eff} , is 1. Nonetheless, a lengthy sequence of intermediate operations can cause memory to become a major limiting factor.

4.1. Comparison with NEO

In this section, we will benchmark the DESC bounce-averaging operator by comparing the neoclassical transport metric $\epsilon_{\text{eff}}^{3/2}$ between the DESC and the neoclassical transport code NEO. For this, we choose the standard W7-X equilibrium given in the desc/examples directory in the DESC repository. The comparison plots are provided in figure 2. For this comparison, the spectral resolution used by DESC for the map from toroidal coordinates to field line coordinates is $N_\alpha = 32, N_\zeta = 64$. The surface average is approximated with $N_l = 32$ toroidal transits. The quadrature resolutions are $N_{b'} = 100, N_q = 50$.

The results match well with a minor discrepancy around $\rho = 0.5$ and the magnetic axis $\rho = 0$. The difference can be attributed to the accuracy of the bounce integrals. We ensure that the bounce integrals are spectrally accurate. Moreover, unlike the NEO code, we do not have to perform a Boozer transform before calculating the bounce integrals. Avoiding a Boozer transformation could be another source of the minor mismatch.

After implementing the calculation of the neoclassical coefficients, in the next section, we will perform optimization to optimize stellarators against neoclassical transport.

5. Optimizing stellarators for reduced neoclassical transport

Here we show a simple optimization example starting from a finite- β helically omnigenous (OH) equilibrium taken from Gaur *et al.* (2024). The parameter $\beta = 2\mu_0 p/B^2$ is the ratio of the plasma pressure to the magnetic pressure. We target flux surfaces near the boundary to reduce the effective ripple while maintaining reasonable elongation and curvature. The objective function minimized by DESC

$$\mathcal{F} = A f_{\text{aspect}}^2 + C f_{\text{curv}}^2 + E f_{\text{elongation}}^2 + R f_{\text{ripple}}^2 \quad (5.1)$$

contains multiple quadratic penalty terms. The definitions of the curvature and elongation objectives are given in Appendix D of Gaur *et al.* (2024). Using DESC, we then perform optimization and minimizes \mathcal{F} while ensuring ideal MHD force balance 2.3 in the existing

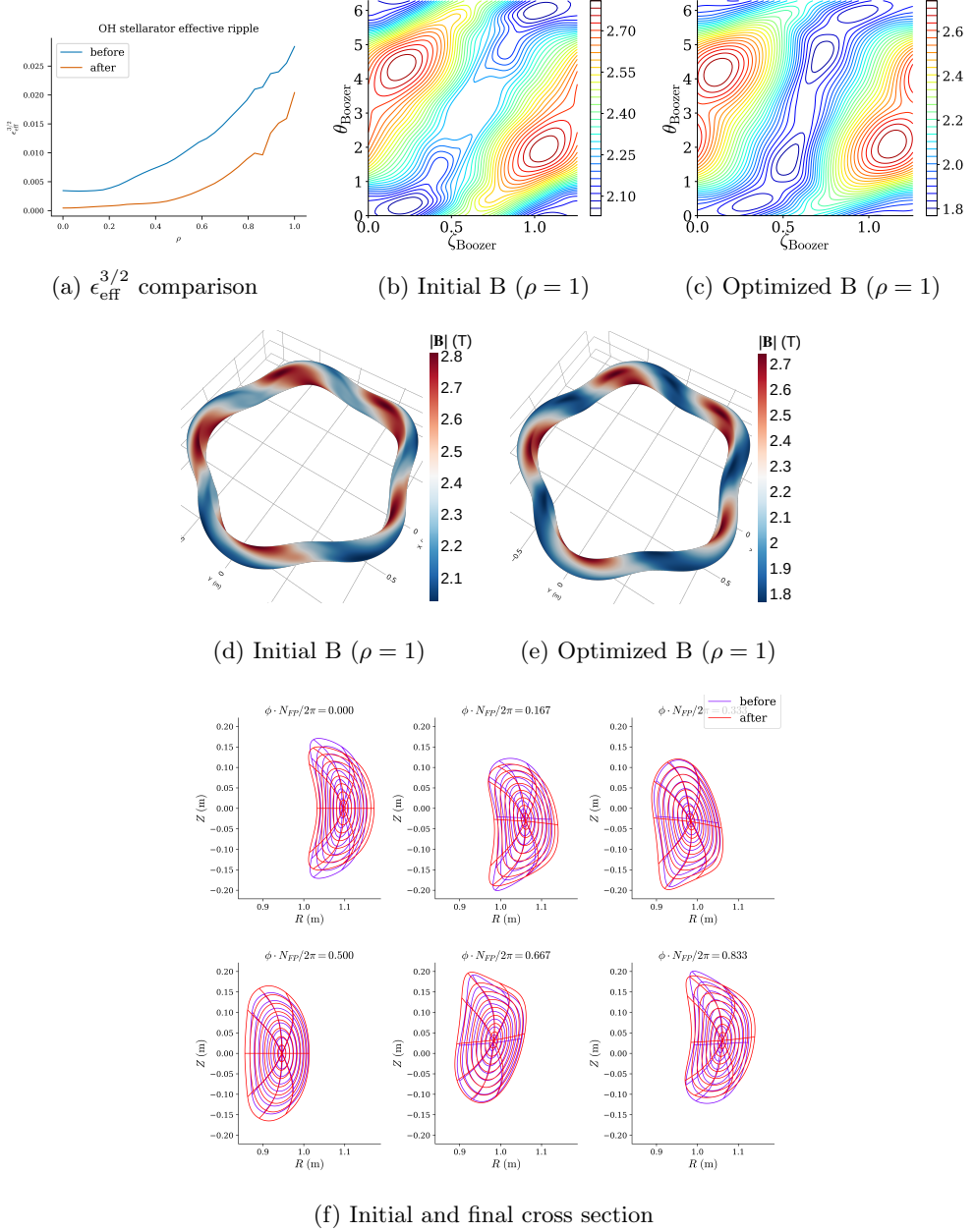


Figure 3: Outputs from the OH transport optimization in DESC.

equilibrium.

$$\min \mathcal{F}(\mathbf{p}), \quad \text{s.t.} \quad \nabla \left(\mu_0 p + \frac{B^2}{2} \right) - \mathbf{B} \cdot \nabla \mathbf{B} = 0, \quad (5.2)$$

where \mathbf{p} represents a set of parameters that determine the pressure, rotational transform profiles, and boundary shape coefficients. A single optimization takes less than two hours on an NVIDIA A100 GPU (NVIDIA Corporation 2020). The initial and optimized results are presented in figure 3.

6. Summary and Conclusions

In this work, we implemented a spectrally accurate, reverse-mode differentiable, bounce-averaging operator in the DESC stellarator optimization suite. Using this, we derived and benchmarked the neoclassical transport proxy $\epsilon_{\text{eff}}^{3/2}$ in section 3 and section 4, respectively. We explained how reverse-mode calculation is faster than forward-mode gradient calculation. Finally, in section 5, we optimize a finite- β configuration for reduced neoclassical transport using reverse-mode differentiation in DESC.

Many objectives of interest rely on bounce-averaging. Quantities such as the second adiabatic invariant $J_{\parallel} = \oint d\ell v_{\parallel}$, $\max(J_{\parallel})$, proxies for gyrokinetic turbulence such as the available energy Mackenbach *et al.* (2022), a proxy for trapped-electron mode turbulence, and new proxies for energetic particle transport Velasco *et al.* (2021). Future work Hibbard *et al.* (2024) would involve demonstrating optimization for energetic particle confinement in DESC.

Acknowledgements This work is funded through the SciDAC program by the US Department of Energy, Office of Fusion Energy Science, and Office of Advanced Scientific Computing Research under contract No. DE-AC02-09CH11466, DE-SC0022005, and Field Work Proposal No. 1019, and the Peter B. Lewis Fund for Student Innovation in Energy and the Environment. This research also used the computing resources of the Della cluster at Princeton University.

Appendix A. Numerical method

The implementation is written in Python using Google’s JAX library Bradbury *et al.* (2018) and is simultaneously compatible with the scientific computing packages `jax.numpy` and `numpy`, taking advantage of the easy readability and maintainability of Python code, while ensuring that the computational operations are performed efficiently. JIT compilation in JAX is used to compile the Python code into machine code at runtime to recover similar performance to low-level programming languages.

A.1. Bounce integral

The bounce averaged drift between the bounce points $\zeta_1(w)$ and $\zeta_2(w)$ of magnetic well w where the parallel velocity of the particle vanishes $|v_{\parallel}|(\zeta_i) = 0$ for $i \in \{1, 2\}$ is given by

$$\langle v_{\text{drift}} \rangle = \frac{\int_{t(\zeta_1)}^{t(\zeta_2)} v_{\text{drift}} dt}{\int_{t(\zeta_1)}^{t(\zeta_2)} dt} \quad (\text{A } 1)$$

Instead of integrating over the trajectory of the particle, the integrals are approximated as line integrals between bounce points by parameterizing time as the distance along a field-line following coordinate, that is $dt = d\ell/|v_{\parallel}|$. We may write $d\ell/|B| = d\zeta/(\mathbf{B} \cdot \nabla\zeta) = d\zeta/B^{\zeta}$ for any coordinate ζ , where the latter relation is the definition of the contravariant basis vector. For particles with magnetic moment μ and energy defined up to some constant $E = \mu|B| + m|v_{\parallel}|^2/2$, it follows that

$$|v_{\parallel}| = \sqrt{2(E - \mu|B|)/m} = \sqrt{2E/m} \sqrt{1 - \mu|B|/E} = \sqrt{2E/m} \sqrt{1 - \lambda|B|} \quad (\text{A } 2)$$

where we have defined the pitch angle $\lambda = \mu/E$. The integral becomes

$$\langle v_{\text{drift}} \rangle = \frac{\int_{\zeta_1}^{\zeta_2} \frac{v_{\text{drift}}}{\sqrt{1 - \lambda|B|}} \frac{|B|}{B^{\zeta}} d\zeta}{\int_{\zeta_1}^{\zeta_2} \frac{1}{\sqrt{1 - \lambda|B|}} \frac{|B|}{B^{\zeta}} d\zeta} \quad (\text{A } 3)$$

where the bounce points ζ_i depend on the particle's pitch λ and $|B|$ such that $\lambda|B|(\zeta_i) = 1$. By conservation of the first adiabatic invariant and the monoenergetic approximation, the pitch angle λ is taken to be a constant.

These optimization proxies are surface averaged functions of bounce integrals, so they require computation of a set of such integrals throughout the plasma volume.

$$\mathcal{F} = \{F(\rho, \alpha, \lambda, w) \mid 1/\lambda \in (\min|B|, \max|B|)\} \quad (\text{A } 4)$$

$$F(\rho, \alpha, \lambda, w) = \int_{\zeta_1(w)}^{\zeta_2(w)} f(\rho, \alpha, \lambda, \zeta, \{G_i(\rho, \alpha, \zeta)\}) d\zeta \quad (\text{A } 5)$$

where f denotes some composition operator on a set of smooth functions $\{G_i\}$. Often $|(\partial f/\partial \zeta)_{\rho, \alpha, \lambda}| \rightarrow \infty$ as ζ approaches the integration boundary. In an axisymmetric device, field line integration over a single poloidal transit is sufficient to capture a surface integral. For a 3D configuration, convergence occurs in the limit of an infinite number of transits for an irrational magnetic surface. For a rational or near-rational surface, it is necessary to average over multiple field lines until the surface is covered sufficiently. Hence, $|\mathcal{F}|$ is infinite in general. The accurate estimation of these many locally defined singular bounce integrals makes evaluation of such proxies more expensive than typical proxies.

A.1.1. Cost

Evaluating a general series expansion with c coefficients at n non-uniform evaluation points has a cost of $\mathcal{O}(cn)$. For a computation on s flux surfaces, where the field line traced on each flux surface has w magnetic wells for each of p pitch angles, there will be swp bounce integrals to compute. With q quadrature points for each integration, the integrand is evaluated at $swpq \sim 10^8$ points. The parameterization of f in (ρ, α, ζ) coordinates is typically not known a priori because the contours of integration change at each optimization step. With an additional t Newton iterations to solve for the coordinate mapping $\theta(\rho, \alpha, \zeta)$ to evaluate f under a known parameterization, $f(\rho, \theta, \zeta, \lambda)$, the computation cost becomes $\mathcal{O}(tcswpq)$. Furthermore, automatic differentiation of the objective with respect to the optimizable parameters incurs an expense that is linear in the problem size. These costs make it necessary to develop an efficient algorithm.

A.2. Function approximation

DESC solves the inverse equilibrium problem. The computational domain is parameterized by the curvilinear toroidal coordinates $(\rho, \theta, \zeta) \in [0, 1] \times \mathbb{R} \times \mathbb{R}$ where ρ is a function of the toroidal flux ψ and θ, ζ are arbitrary angles. These coordinates are related to the Clebsch coordinates (ψ, α, ζ) defined by $B = \nabla\psi \times \nabla\alpha$ through the maps

$$\alpha: \rho, \theta, \zeta \mapsto \vartheta(\rho, \theta, \zeta) - \bar{t}(\rho)\phi(\rho, \theta, \zeta) \quad (\text{A } 6)$$

$$\vartheta: \rho, \theta, \zeta \mapsto \theta + \lambda(\rho, \theta, \zeta) \quad (\text{A } 7)$$

$$\phi: \rho, \theta, \zeta \mapsto \zeta + \omega(\rho, \theta, \zeta) \quad (\text{A } 8)$$

where λ, ω are poloidal, toroidal stream functions, respectively, and \bar{t} is the rotational transform normalized by 2π . The stream functions relate the angles θ, ζ that parameterize the plasma boundary $R(\theta, \zeta), Z(\theta, \zeta)$ with those that make the magnetic field lines straight in the ϑ, ϕ plane. Fourier-Zernike series expansions, with coefficients determined by the optimizer, approximate the stream functions λ and ω .

The optimization proxies that involve bounce averaging are typically nonlinear functions of distance along field lines between bounce points, and this requires that the surface average be performed by integration along curves of constant ρ and α . Computing the

values θ along a field line denoted by (ρ_i, α_i) requires solving a nonlinear relation pointwise for the θ^* values which satisfy

$$\alpha(\rho_i, \theta^*, \zeta) = \alpha_i \quad (\text{A } 9)$$

The solution to this relation is unique, and it is best found with Newton iteration. To avoid repeating this expensive root-finding problem at each quadrature point, the inverse map of (A 6) is estimated. Recall, the frequency transform of the map $\rho, \alpha, \zeta \mapsto \theta(\rho, \alpha, \zeta)$ under the chosen basis must be concentrated at low frequencies for the series to converge fast. For periodic (non-periodic) maps, the standard choice for the basis is a Fourier (Chebyshev) series [Boyd \(2013\)](#). Both converge exponentially for smooth maps, but the larger region of convergence in the complex plane of Fourier series make it preferable to choose coordinate systems such that the function to approximate is periodic. The Chebyshev polynomials are preferred to other orthogonal polynomial series since fast discrete polynomial transforms (DPT) are implemented via fast transform to Chebyshev then DCT. Although nothing prohibits a direct DPT, we want to rely on existing libraries. Therefore, (A 9) is solved on a fixed tensor-product grid in $(\rho, \alpha, \zeta) \in [0, 1] \times [0, 2\pi]^2$ on the Fourier nodes in α and Chebyshev nodes in ζ . These values $\theta(\rho, \alpha, \zeta)$ on each flux surface are interpolated to a Fourier-Chebyshev series by the real FFT and DCT.

$$\theta: \rho, \alpha, \zeta \mapsto \sum_{mn} t_{mn}(\rho) \exp(im\alpha) T_n(\zeta) \quad (\text{A } 10)$$

Partial summation techniques are used to increase evaluation speed. When the optimizer perturbs the spectral coefficients of the stream functions, the root-finding in (A 6) will be initialized with the previous solution.

It should be noted that (A 10) estimates the inverse map of (A 6) over a single branch cut of α . That is, the expansion for θ above will differ depending on the value of $k \in \mathbb{Z}$ that determines the domain for $\alpha \in [2\pi k, 2\pi(k+1))$. This follows from the definition of α in $B = \nabla\psi \times \nabla\alpha$ on an irrational magnetic surface which implies the angle $\theta(\rho, \alpha, \zeta)$ is multivalued at a physical location. In particular, following an irrational field, the single-valued $\theta \in \mathbb{R}$ grows unbounded as $|\zeta| \rightarrow \infty$. Therefore, it is impossible to approximate the map $\rho, \alpha, \zeta \mapsto \theta(\rho, \alpha, \zeta)$ using single-valued basis functions defined on a compact set as such an approximation attains a finite maximum. Likewise, α is multivalued. As the field line is followed, the label may jump to $\alpha \notin [2\pi k, 2\pi(k+1))$ after completing some toroidal transit. Hence, $\theta(\rho, \alpha, \zeta)$ must be periodic in α with period 2π . At every point $\zeta_p \in [2\pi k, 2\pi\ell]$ where $k, \ell \in \mathbb{Z}$ where the field line completes a poloidal transit there is guaranteed to exist a discrete jump discontinuity in the approximation for θ at $\zeta = 2\pi\ell(p)$, starting the toroidal transit. Still, it suffices to interpolate θ over one branch cut. To recover the single-valued θ from the Fourier-Chebyshev interpolation over one branch cut, at $\zeta = 2\pi k$ for every $k \in \mathbb{Z}$ we can add an integer multiple of 2π to the next cut of θ .[†]

A.3. Off-grid interpolation

The Zernike polynomials are orthogonal basis functions on the unit disc. The 2D coupling of this basis is designed to concentrate the frequency transform of maps on the unit disc at lower frequencies than geometry-agnostic tensor-product basis such as

[†] A necessary condition for recovering the true θ from its interpolation over one branch cut is for the approximation to not enforce $\theta(\rho, \alpha, \zeta) = \theta(\rho, \alpha, \zeta + 2\pi k)$ for $k \in \mathbb{Z}$. For this reason, the map $\rho, \alpha, \zeta \mapsto \theta(\rho, \vartheta(\rho, \alpha, \zeta), \zeta)$ is not interpolated with Fourier series in ϑ, ζ because it is impossible to approximate an unbounded function with a finite Fourier series. Due to Gibbs effects, this statement holds even when the goal is to approximate θ over one branch cut. The proof uses analytic continuation.

Fourier-Chebyshev. Boyd shows the required number of spectral coefficients is typically half that of Fourier-Chebyshev [Boyd & Yu \(2011\)](#). Therefore, an optimization that varies a finite number of coefficients in the Fourier-Zernike series expansions for R, Z, λ, ω at a time will have more freedom compared to expansions under other basis. However, fast transforms such as FFTs and DCTs, and their approximate non-uniform generalizations, cannot interpolate this basis as they can the Fourier-Chebyshev basis.

Because the contours of the magnetic field lines vary throughout an optimization, optimization of these objectives necessarily involves “off-grid” interpolation, or evaluation of transforms on irregular non-uniform grids ([Boyd 2013](#), section 10.7). In our case, the locally defined and singular nature of the bounce integrals demands that the evaluation grid be non-uniform while the optimization objective further requires this grid to be time-dependent. Such interpolation dominates the cost of pseudo-spectral codes for the cost of evaluation $\mathcal{O}(cn)$ of a series with c coefficients at n points contains a large proportionality constant if the basis functions cannot be precomputed. For a 3D basis, the number of spectral coefficients c is large. For Zernike polynomials, inability to precompute the basis functions is a handicap. Therefore, it is best to reduce the dimensionality of the series expansions.

The implemented algorithm computes the Fourier-Zernike basis functions prior to the optimization on a fixed tensor-product grid in (ρ, θ, ζ) with uniformly spaced nodes in $(\theta, \zeta) \in [0, 2\pi) \times [0, 2\pi/\text{NFP})$ where NFP denotes the discrete integer periodicity of the boundary in $(\theta, \zeta) \in [0, 2\pi)^2$ coordinates. The smooth periodic maps $\{G_i\}$ in the integrands of the bounce integrals are computed on this grid through evaluation of R, Z, λ, ω . These values are interpolated to a double Fourier series in $(\theta, \zeta) \in [0, 2\pi) \times [0, 2\pi/\text{NFP})$ by the real Fourier transform. This foots the cost by reducing the number of spectral coefficients, replacing Zernike polynomials with the complex exponential basis functions which are cheaper to evaluate, and bypassing the operations to compute $\{G_i\}$ from R, Z, λ, ω .[†]

The maps $\{G_i\}$ are evaluated at the quadrature points from these Fourier series using the type two non-uniform fast transforms, enabling evaluation of a series with c coefficients at n points with cost $\mathcal{O}(-(c+n)\log(c)\log(\epsilon)) \ll \mathcal{O}(cn)$.[‡] Non-uniform transforms are used to solve the off-grid interpolation bottleneck as opposed to the methods that involve upsampling then interpolation with local splines ([Boyd 2013](#), section 10.7) to preserve spectral accuracy. Local spline interpolation is also less efficient as NFP increases. High order accuracy of $|B|$ in particular is preferred for accurate estimation of these proxies because the bounce integrals are strong functions of $|B|$.

A.4. Quadrature

To compute the bounce points, we find the solutions $\zeta_k(\rho, \alpha, \lambda)$ to $\lambda|B|(\rho, \alpha, \zeta_k) = 1$. We evaluate the Fourier series of the magnetic field strength at the optimal points along field lines for interpolation with either local splines or piecewise Chebyshev series. Either function approximation enables global root-finding algorithms to obtain the ζ_k . The points ζ_k are polished with one application of secant method using the Fourier series $|B|$. The periodic smooth components of the integrand are interpolated to the quadrature points with non-uniform FFTs.

$$G: \rho, \alpha, \zeta \mapsto \sum_{mn} g_{mn}(\rho) \exp(i[m\theta(\rho, \alpha, \zeta) + n\zeta]) \quad (\text{A } 11)$$

[†] Recomputing the 3D Fourier-Zernike transforms in DESC at each optimization step was found to dominate runtime and memory consumption.

[‡] ϵ is an interpolation error term that is implementation dependent, but it always lies inside a logarithm.

High-order quadratures estimate (A 5) after resolving the singularity. Bounce integrals with bounce points where the derivative of $|B|$ does not vanish have $1/2$ power law singularities. However, strongly singular integrals where the domain of the integral ends at the local extrema of $|B|$ are not integrable. Hence, everywhere except for the extrema, a Chebyshev or Legendre quadrature discussed below captures the integral because $\sqrt{(1-\zeta^2)}/\sqrt{1-\lambda|B|(\zeta)} \sim h(\zeta, \lambda)$ is smooth in ζ . The clustering of the nodes near the singularities is sufficient to estimate $h(\zeta, \lambda)$.

A.4.1. Gauss-Legendre under sin transformation

Gaussian quadrature methods approximate the integral

$$\int_{-1}^1 w(x)f(x) dx \approx \sum_k W_k f(x_k) \quad (\text{A } 12)$$

for some weight function w positive and continuous on $(-1, 1)$, by replacing f with its Hermite interpolation polynomial and construct the quadrature to not require evaluation of df/dx . To estimate singular integrals, a change of variable whose Jacobian decays to zero slowly near the singularity can transform the integrand into a well-behaved function that can be approximated by a polynomial. It is important that the transformation accounts exactly for the order of the singularity to prevent unnecessary clustering of quadrature points. For bounce integrals, we define $\mathbb{D} = [-1, 1]$

$$b: \begin{cases} \mathbb{D} \rightarrow [\zeta_1, \zeta_2] \\ x \mapsto (x+1)(\zeta_2 - \zeta_1)/2 + \zeta_1 \end{cases} \quad (\text{A } 13)$$

$$a: \begin{cases} \mathbb{D} \rightarrow \mathbb{D} \\ x \mapsto \sin(\pi x/2) \end{cases} \quad (\text{A } 14)$$

and define x such that $b(a[x]) = \zeta$, so that the integral in (A 5) becomes

$$H = \int_{\zeta_1}^{\zeta_2} h(\zeta) d\zeta = \int_{-1}^1 h(b(a[x])) \frac{db}{da} \frac{da}{dx} dx \quad (\text{A } 15)$$

Now Gauss-Legendre quadrature in the coordinate x can estimate bounce integrals. Empirically, this quadrature tends to be more robust to function approximation error than Gauss-Chebyshev of the first kind on integrals with strong singularities.

Appendix B. Quadrature comparison

We compare the following quadratures methods to calculate bounce averages for simple cases such as incomplete elliptic integrals of the first and second kind and “W”-shaped wells.

- (i) Uniform trapezoidal
- (ii) Simpson’s 3/8
- (iii) $\tanh - \sinh$ double exponential (DE)
- (iv) Gauss-Chebyshev of the first (GC₁) and second kind (GC₂)
- (v) Gauss-Legendre (GL) with a sin transformation

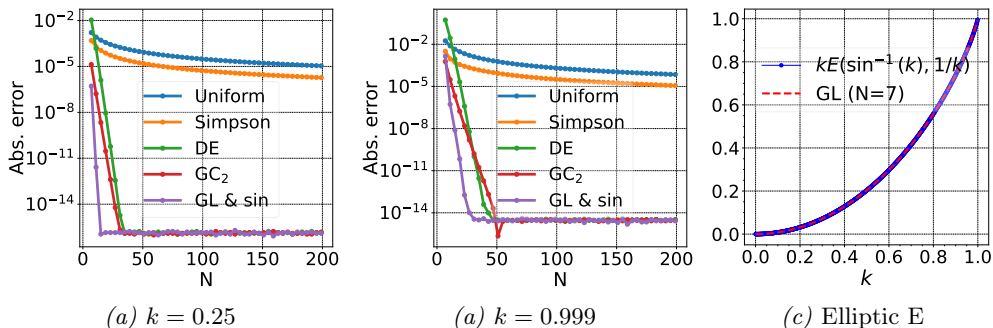


Figure 4: Comparison of various quadrature methods used to calculate the incomplete elliptic integral of the first kind. Gauss-Chebyshev, Gauss-Legendre, and double exponential quadrature show exponential convergence whereas the Uniform and Simpson quadratures hit floating point plateaus early.

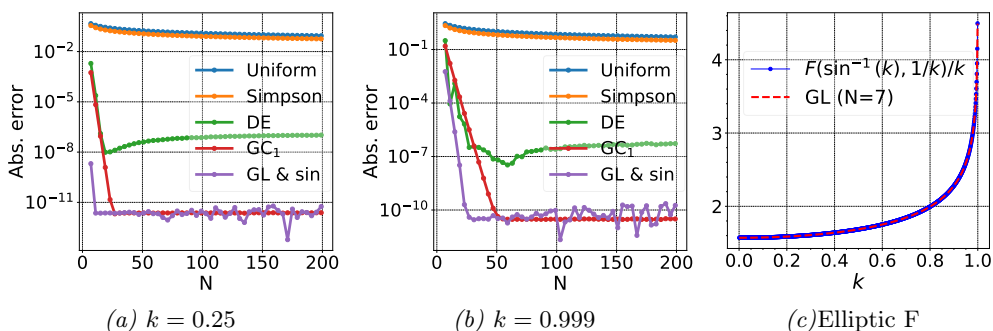


Figure 5: Comparison of various quadrature methods used to calculate the incomplete elliptic integral of the second kind. Gauss-Chebyshev, Gauss-Legendre quadratures show exponential convergence whereas Uniform, Simpson, and double exponential quadratures hit floating point plateaus early.

$$F\left(\sin^{-1}(k), \frac{1}{k}\right) / k \equiv \int_0^{\sin^{-1}(k)} d\zeta \frac{1}{\sqrt{k^2 - \sin(\zeta)^2}} = K(k) \quad (\text{B } 1)$$

$$kE\left(\sin^{-1}(k), \frac{1}{k}\right) \equiv \int_0^{\sin^{-1}(k)} d\zeta \sqrt{k^2 - \sin(\zeta)^2} = E(k) + (k^2 - 1)K(k) \quad (\text{B } 2)$$

The last equality in (B 1) comes from (C 15) and (B 2) comes from (C 16). To understand the performance of the quadratures in a more realistic magnetic field for stellarators, we construct two simple “W”-shaped wells in Figures 6 and 7 and compute $\int_{-1}^1 d\zeta f(\zeta)$ where $f(\zeta)$ is $1/\sqrt{2 - |B|(\zeta)}$ or $\sqrt{2 - |B|(\zeta)}$, corresponding to a strong and weak singularity, respectively.

Automatically differentiable bounce-averaging

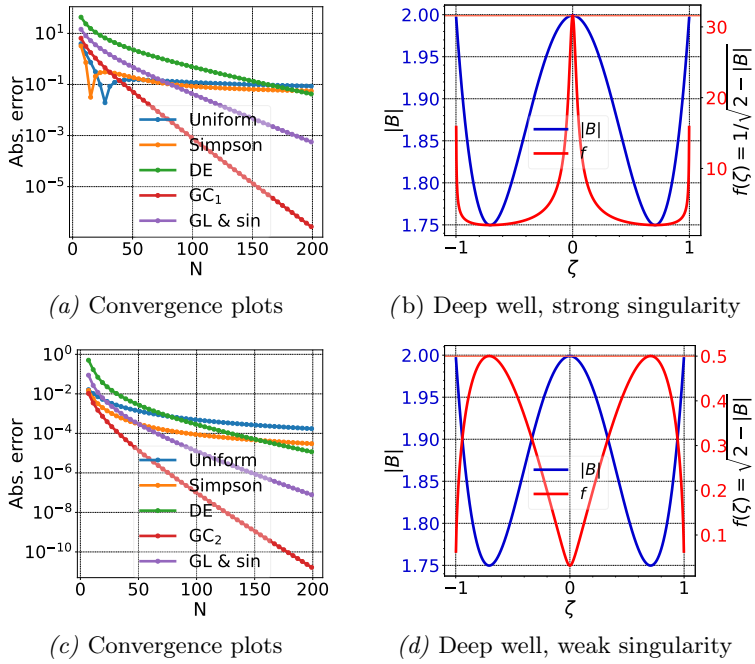


Figure 6: Quadrature comparison for deep “W”-shaped wells.

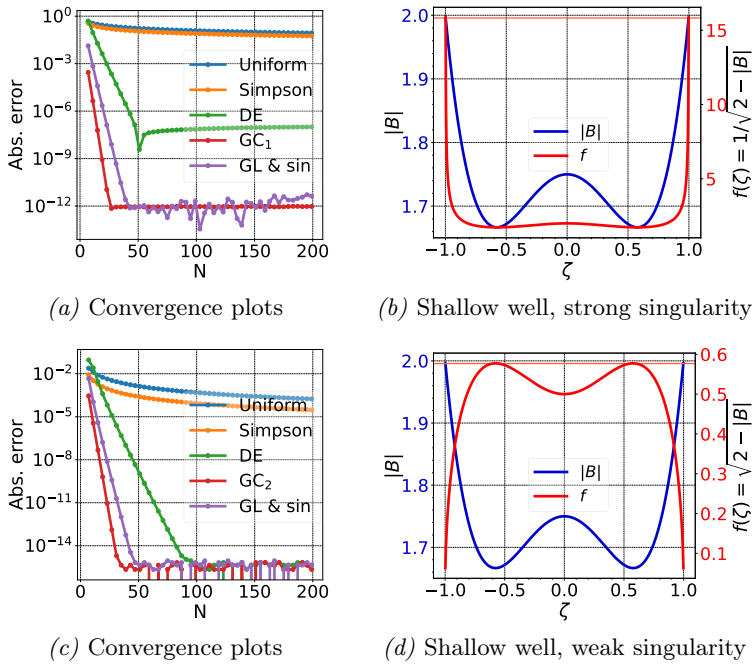


Figure 7: Quadrature comparison for shallow “W”-shaped wells.

Appendix C. Bounce-averaged drifts in shifted-circle model

In a shifted-circle model for plasma equilibrium, we can approximately solve for analytic expressions for bounce averaged drifts. In this model, the magnetic field can be written

$$\mathbf{B} = F\nabla\phi + \frac{d\psi}{dr} \frac{r}{R_0} \nabla\vartheta \quad (\text{C1})$$

where F is the enclosed poloidal current, ψ is poloidal flux, and ϑ is a field line following coordinate. To first order, the poloidal field can be ignored and the magnetic field strength can be written as $|B| = B_0(1 - \epsilon \cos(\vartheta))$, where $\epsilon = r/R_0$ is the inverse aspect ratio. The geometric coefficients are defined below.

$$\text{gradpar} = \mathbf{b} \cdot \nabla\vartheta = G_0(1 - \epsilon \cos \vartheta) \quad (\text{C2})$$

where $\epsilon \ll 1$ is the aspect ratio of the flux surface of interest. The integrated local shear labeled by gds21, with \hat{s} defining the global shear, is

$$\hat{s} = -\frac{\rho}{\iota} \frac{d\iota}{d\rho} \quad (\text{C3})$$

$$\alpha_{\text{MHD}} = -\frac{0.5}{\iota^2} \frac{dP}{d\rho} \quad (\text{C4})$$

$$\text{gds21} = \frac{\nabla\psi \cdot \nabla\alpha}{|\nabla\psi|^2} = -\hat{s} \left(\hat{s}\vartheta - \frac{\alpha_{\text{MHD}}}{|B|^4} \sin\vartheta \right) + \mathcal{O}(\epsilon) \quad (\text{C5})$$

and the binormal component of the $\nabla|B|$ drift

$$(\nabla|B|)_{\text{drift}} = \frac{1}{|B|^3} (\mathbf{B} \times \nabla|B|) \cdot \nabla\alpha \quad (\text{C6})$$

$$\begin{aligned} &= f_2 \left[-\hat{s} + \left(\cos\vartheta - \frac{\text{gds21}}{\hat{s}} \sin\vartheta \right) \right] \\ &= f_2 \left[-\hat{s} + \left(\cos\vartheta + \hat{s}\vartheta \sin\vartheta - \frac{\alpha_{\text{MHD}}}{B_0^4} \sin(\vartheta)^2 \right) \right] + \mathcal{O}(\epsilon) \end{aligned} \quad (\text{C7})$$

where we have used (C5) to obtain the final expression for $(\nabla|B|)_{\text{drift}}$. The geometric factor corresponding to the binormal component of the curvature drift is

$$\text{cvdrift} = \frac{1}{|B|^3} [\mathbf{B} \times \nabla(p + |B|^2/2)] \cdot \nabla\alpha \quad (\text{C8})$$

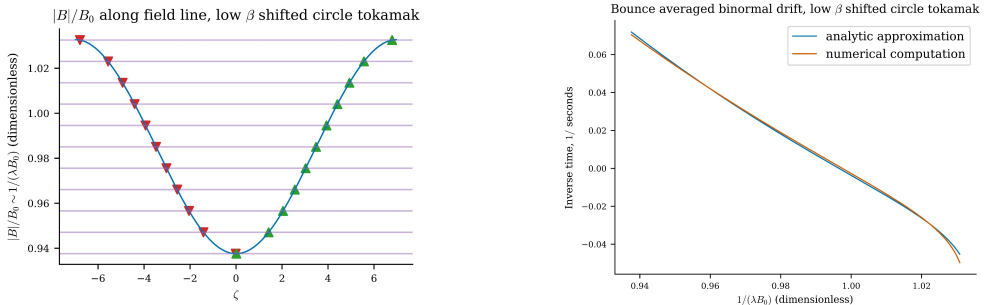
$$= (\nabla|B|)_{\text{drift}} + f_3 \frac{1}{|B|^3} \frac{dP}{d\rho} \quad (\text{C9})$$

$$= f_2 \left[-\hat{s} + \left(\cos\vartheta + \hat{s}\vartheta \sin\vartheta - \frac{\alpha_{\text{MHD}}}{B_0^4} \sin(\vartheta)^2 \right) \right] + f_3 \frac{\alpha_{\text{MHD}}}{B_0^2} + \mathcal{O}(\epsilon) \quad (\text{C10})$$

The quantities f_2 and f_3 are scalar factors which contain a number of constants. Denoting w as the velocity of the particle, the bounce-averaged drift can now be computed as

$$\langle \omega_{\text{Ds}} \rangle = \left(\int_{\vartheta_{b1}}^{\vartheta_{b2}} \frac{d\vartheta}{\mathbf{b} \cdot \nabla\vartheta} \frac{1}{|w_{\parallel}|} \right)^{-1} \int_{\vartheta_{b1}}^{\vartheta_{b2}} \frac{d\vartheta}{\mathbf{b} \cdot \nabla\vartheta} \frac{1}{|w_{\parallel}|} \left[|w_{\parallel}|^2 \text{cvdrift} + \frac{|w_{\perp}|^2}{2} (\nabla|B|)_{\text{drift}} \right] \quad (\text{C11})$$

where ϑ_{b1} and ϑ_{b2} are bounce angles. As used in Connor *et al.* and shown by Hegna, in the limit of a large aspect ratio shifted circle model, the parallel speed of a particle with



(a) For a given pitch marked by a horizontal line, $|v_{\parallel}| = 0$ at the bounce points marked by triangles.

(b) Binormal drift.

Figure 8: In a shifted-circle model, we can approximately solve for analytic expressions for bounce averaged drifts and test the accuracy of the bounce averaging.

a fixed energy E is

$$\begin{aligned}
 |w_{\parallel}| &= \sqrt{\frac{2E}{m}} \sqrt{1 - \lambda|B|} \\
 &= \sqrt{\frac{2E}{m}} \sqrt{1 - \lambda B_0(1 - \epsilon \cos \vartheta)} \\
 &= \sqrt{\frac{2E}{m}} \sqrt{2\epsilon\lambda B_0} \sqrt{k^2 - \sin(\vartheta/2)^2}
 \end{aligned} \tag{C 12}$$

where $\lambda = \mu/E$ is the pitch angle, $\mu = m|w_{\perp}|^2/(2|B|)$ is the magnetic moment, $E = m|w|^2/2$ the particle energy, and the parameter

$$k^2 = \frac{1}{2} \left(\frac{1 - \lambda B_0}{\epsilon\lambda B_0} + 1 \right) \tag{C 13}$$

is a reparametrization of the pitch angle λ . Using these geometric simplifications, and $|w_{\perp}|^2/2 = E - |w_{\parallel}|^2/2$, we can write the bounce-averaged drift as

$$\begin{aligned}
 \langle \omega_D \rangle &= \left(\int_{-2 \sin^{-1}(k)}^{2 \sin^{-1}(k)} \frac{d\vartheta}{\mathbf{b} \cdot \nabla \vartheta} \frac{1}{\sqrt{2\epsilon\lambda B_0}} \frac{1}{\sqrt{k^2 - (\sin(\vartheta/2))^2}} \right)^{-1} \\
 &\quad \int_{-2 \sin^{-1}(k)}^{2 \sin^{-1}(k)} \frac{d\vartheta}{\mathbf{b} \cdot \nabla \vartheta} \left[\sqrt{2\epsilon\lambda B_0} \sqrt{k^2 - (\sin(\vartheta/2))^2} \text{cvdrift} \right. \\
 &\quad \left. - \sqrt{2\epsilon\lambda B_0} \frac{\sqrt{k^2 - (\sin(\vartheta/2))^2}}{2} (\nabla|B|)_{\text{drift}} \right. \\
 &\quad \left. + \frac{1}{\sqrt{2\epsilon\lambda B_0}} \frac{1}{\sqrt{k^2 - (\sin(\vartheta/2))^2}} \frac{(\nabla|B|)_{\text{drift}}}{2} \right]
 \end{aligned} \tag{C 14}$$

Using the following identities, we can further simplify (C 14). The incomplete elliptic integrals are converted to complete elliptic integrals using the Reciprocal-Modulus

transformation (first two relations below) (Olver *et al.* 2024).

$$l_0 = \int_{-2 \sin^{-1}(k)}^{2 \sin^{-1}(k)} \frac{d\vartheta}{\sqrt{k^2 - \sin(\vartheta/2)^2}} = 4K(k) \quad (\text{C } 15)$$

$$l_1 = \int_{-2 \sin^{-1}(k)}^{2 \sin^{-1}(k)} d\vartheta \sqrt{k^2 - \sin(\vartheta/2)^2} = 4 [E(k) + (k^2 - 1)K(k)] \quad (\text{C } 16)$$

$$l_2 = \int_{-2 \sin^{-1}(k)}^{2 \sin^{-1}(k)} \frac{d\vartheta}{\sqrt{k^2 - \sin(\vartheta/2)^2}} \vartheta \sin(\vartheta) = 8kE \quad (\text{C } 17)$$

$$\begin{aligned} l_3 &= \int_{-2 \sin^{-1}(k)}^{2 \sin^{-1}(k)} d\vartheta \sqrt{k^2 - \sin(\vartheta/2)^2} \vartheta \sin(\vartheta) \\ &= \frac{8k}{9} [2(-1 + 2k^2)E - (-1 + k^2)K] \end{aligned} \quad (\text{C } 18)$$

$$\begin{aligned} l_4 &= \int_{-2 \sin^{-1}(k)}^{2 \sin^{-1}(k)} \frac{d\vartheta}{\sqrt{k^2 - \sin(\vartheta/2)^2}} (\sin(\vartheta))^2 \\ &= \frac{8k}{3} [(-1 + 2k^2)E - 2(-1 + k^2)K] \end{aligned} \quad (\text{C } 19)$$

$$\begin{aligned} l_5 &= \int_{-2 \sin^{-1}(k)}^{2 \sin^{-1}(k)} d\vartheta \sqrt{k^2 - \sin(\vartheta/2)^2} (\sin(\vartheta))^2 \\ &= \frac{32k}{30} [2(1 - k^2 + k^4)E - (1 - 3k^2 + 2k^4)K] \end{aligned} \quad (\text{C } 20)$$

$$\begin{aligned} l_6 &= \int_{-2 \sin^{-1}(k)}^{2 \sin^{-1}(k)} \frac{d\vartheta}{\sqrt{k^2 - \sin(\vartheta/2)^2}} \cos(\vartheta) \\ &= \frac{4}{3} [(2k^2 - 1)E + (2k^2 - 3)(k^2 - 1)K] \end{aligned} \quad (\text{C } 21)$$

$$\begin{aligned} l_7 &= \int_{-2 \sin^{-1}(k)}^{2 \sin^{-1}(k)} d\vartheta \sqrt{k^2 - \sin(\vartheta/2)^2} \cos(\vartheta) \\ &= [8E - 4K] \end{aligned} \quad (\text{C } 22)$$

where K and E are complete elliptic integrals of the first and second kind, respectively. Using these formulae, to lowest order, we can write all the three terms in the above equation, and the analytical bounce-averaged drifts give us

$$\begin{aligned} \langle \omega_D \rangle &= \frac{1}{G_0} \left\{ \left(f_3 \frac{\alpha_{\text{MHD}}}{B_0^2} - f_2 \frac{\hat{s}}{2} \right) l_1 + \frac{f_2}{2} \left(\hat{s} l_3 - \frac{\alpha_{\text{MHD}}}{B_0^4} l_5 + l_7 \right) \right. \\ &\quad \left. + \frac{f_2}{2} \left[-\hat{s} (l_0 - l_2) - \frac{\alpha_{\text{MHD}}}{B_0^4} l_4 + l_6 \right] \right\} \\ &= \frac{1}{G_0} \left(f_3 \frac{\alpha_{\text{MHD}}}{B_0^2} l_1 - \frac{f_2}{2} \left[\hat{s} (l_0 + l_1 - l_2 - l_3) + \frac{\alpha_{\text{MHD}}}{B_0^4} (l_4 + l_5) - (l_6 + l_7) \right] \right) \end{aligned} \quad (\text{C } 23)$$

In **Figure 8b**, the minor difference is a result of ignoring higher-order terms in the analytic approximation as the shifted circle model is only accurate up to $\mathcal{O}(\epsilon^2)$.

REFERENCES

- BOYD, J.P. 2013 *Chebyshev and Fourier Spectral Methods: Second Revised Edition*. Dover Publications.
- BOYD, JOHN P. & YU, FU 2011 Comparing seven spectral methods for interpolation and for solving the poisson equation in a disk: Zernike polynomials, logan–shepp ridge polynomials, chebyshev–fourier series, cylindrical robert functions, bessel–fourier expansions, square-to-disk conformal mapping and radial basis functions. *Journal of Computational Physics* **230** (4), 1408–1438.
- BRADBURY, JAMES, FROSTIG, ROY, HAWKINS, PETER, JOHNSON, MATTHEW JAMES, LEARY, CHRIS, MACLAURIN, DOUGAL, NECULA, GEORGE, PASZKE, ADAM, VANDERPLAS, JAKE, WANDERMAN-MILNE, SKYE & ZHANG, QIAO 2018 JAX: composable transformations of Python+NumPy programs.
- CONLIN, RORY, DUDT, DANIEL W, PANICI, DARIO & KOLEMEN, EGEMEN 2023 The DESC stellarator code suite. Part 2. Perturbation and continuation methods. *Journal of Plasma Physics* **89**, 955890305.
- D’HAESELEER, W. D., HITCHON, W. N. G., CALLEN, J. D. & SHOHEIT, J. L. 2012 *Flux coordinates and magnetic field structure: a guide to a fundamental tool of plasma theory*. Springer Science & Business Media.
- DREVLAK, M., BEIDLER, C. D., GEIGER, J., HELANDER, P. & TURKIN, Y. 2018 Optimisation of stellarator equilibria with rose. *Nuclear Fusion* **59**, 016010.
- DUDT, DW & KOLEMEN, E 2020 DESC: A stellarator equilibrium solver. *Physics of Plasmas* **27** (10).
- GAUR, RAHUL, CONLIN, RORY, DICKINSON, DAVID, PARISI, JASON F, DUDT, DANIEL, PANICI, DARIO, KIM, PATRICK, UNALMIS, KAYA, DORLAND, WILLIAM D & KOLEMEN, EGEMEN 2024 Omnigenous stellarator equilibria with enhanced stability. *arXiv preprint arXiv:2410.04576* .
- HELANDER, PER 2014 Theory of plasma confinement in non-axisymmetric magnetic fields. *Reports on Progress in Physics* **77** (8), 087001.
- HELANDER, PER & SIGMAR, DIETER J 2005 *Collisional transport in magnetized plasmas*, , vol. 4. Cambridge university press.
- HIBBARD, GRETA, PANICI, DARIO, GAUR, RAHUL, UNALMIS, KAYA & KOLEMEN, EGEMEN 2024 Optimizing stellarators against energetic particle loss with desc. *Bulletin of the American Physical Society* .
- HIRSHMAN, S. P. & WHITSON, J. C. 1983 Steepest-descent moment method for three-dimensional magnetohydrodynamic equilibria. *The Physics of fluids* **26**, 3553.
- LANDREMAN, M., MEDASANI, B., WECHSUNG, F., GIULIANI, A., JORGE, R. & ZHU, C. 2021 SIMSOPT: A flexible framework for stellarator optimization. *Journal of Open Source Software* **6**, 3525.
- LAZERSON, SAMUEL, SCHMITT, JOHN, ZHU, CAO XIANG, BRESLAU, JOSHUA & STELLOPT DEVELOPERS, ALL 2020 Stellopt.
- MACKENBACH, RJJ, PROLL, JOSEFINE HE & HELANDER, P 2022 Available energy of trapped electrons and its relation to turbulent transport. *Physical Review Letters* **128**, 175001.
- NEMOV, VV, KASILOV, SV, KERNBICHLER, W & HEYN, MF 1999 Evaluation of $1/\nu$ neoclassical transport in stellarators. *Physics of plasmas* **6** (12), 4622–4632.
- NVIDIA CORPORATION 2020 Nvidia A100 tensor core gpu. <https://www.nvidia.com/en-us/data-center/a100/>, accessed: 3 December 2024.
- OLVER, F. W. J., OLDE DAALHUIS, A. B., LOZIER, D. W., SCHNEIDER, B. I., BOISVERT, R. F., CLARK, C. W., MILLER, B. R., B. V. SAUNDERS, H. S. COHL & M. A. McCLAIN, EDS. 2024 *NIST digital library of mathematical functions*. <https://dlmf.nist.gov/>, Release 1.2.2 of 2024-09-15.
- PANICI, DARIO, CONLIN, RORY, DUDT, DANIEL W, UNALMIS, KAYA & KOLEMEN, EGEMEN 2023 *The DESC stellarator code suite. Part 1. Quick and accurate equilibria computations*. *Journal of Plasma Physics* **89**, 955890303.
- SPITZER JR, LYMAN 1958 *The stellarator concept*. *The Physics of Fluids* **1**, 253–264.
- VELASCO, JL, CALVO, I, MULAS, S, SÁNCHEZ, E, PARRA, FI, CAPPÀ, A & OTHERS 2021 *A model for the fast evaluation of prompt losses of energetic ions in stellarators*. *Nuclear Fusion* **61**, 116059.